Universal Active Metasurfaces for Ultimate Wavefront Molding by Manipulating the Reflection Singularities

Mahmoud Elsawy,* Christina Kyrou, Elena Mikheeva, Rémi Colom, Jean-Yves Duboz, Khosro Zangeneh Kamali, Stéphane Lanteri, Dragomir Neshev, and Patrice Genevet

Optical metasurfaces are becoming ubiquitous optical components to control light properties. However, most of these devices are passive and cannot be arbitrarily reconfigured according to the change in the surrounding environment. Here the authors propose an innovative design strategy relying on the position of topological singularities to address full phase modulation of light with almost unity efficiency. The active metasurface unit cells consist of asymmetric Gires–Tournois resonators filled with either silicon or hetero-structured materials to leverage on the thermo-optical or electro-optical effects, respectively. In both cases, a full phase modulation associated with 100% reflection amplitude is observed even when dealing with extremely low refractive index change, on the order of 0.01. Improving the deflection efficiencies for each deflection angle is performed by optimizing the refractive index modulation profile in the extended unit cell using an advanced statistical learning optimization methodology. Consequently, active beam steering designs for active thermo-optical effect with ultimate performance exceeding 90% have been optimized. Furthermore, active wavefront splitting using electro-optics materials is optimized to reach ultimate modulation performances with nearly 92% efficiency. The realization of highly efficient active beam-forming operating at high frequencies would open important applications in imaging microscopy, and 3D light detection and ranging (LiDAR).

1. Introduction

Metasurfaces (MSs) are functional optical interfaces composed of subwavelength assemblies of optically thin nanostructured elements.[1–4] The interest in MSs has kept growing continuously for more than a decade, driven by their compatibility with planar semiconductor fabrication technology and their potential for integration into optoelectronic devices. In this context, ultra-compact metasurface-based deflectors, beam splitters, lenses, waveplates, and holograms are approaching unitary wavefront-molding efficiencies.[5–10] Currently, three methods are used to efficiently address the local phase, amplitude, or polarization of light. The first method uses the modification of the effective refractive index (ERI) of low-quality factor truncated nano-waveguides.[3,6,11,12] The second method leverages the Pancharatnam Berry (PB) phase imprinted by birefringent particles on the polarization-converted light.[13–16] Finally, the third phase addressing mechanism relies on the resonant scattering of light and the associated light scattering modulation properties, using plasmonic or dielectric scatterers.[17–20] While the first two methods are presumably well-understood, recent works addressing the last phase modulation method revealed an intriguing connection between the full phase modulation and the topological effects governing the light interaction with resonant nanoparticles.[21] Extending these tuning mechanisms to the active regime would offer real-time and ultra-fast wavefront modulation.[22] Tunable MS are triggering real enthusiasm in the community, driven mainly by their low-cost scalable manufacturing capabilities for large volume applications in active beam steering for light detection and ranging (LiDAR),[23–25] AR/VR

M. Elsawy, S. Lanteri
Université Côte d'Azur
Inria, CNRS
LJAD
06902 Sophia Antipolis Cedex, France
E-mail: mahmoud.elsawy@inria.fr

C. Kyrou, E. Mikheeva, R. Colom, J.-Y. Duboz, P. Genevet
Université Côte d'Azur
CNRS
CRHEA
Rue Bernard Gregory
Sophia Antipolis
06560 Valbonne, France

K. Z. Kamali, D. Neshev
TMOS, Research School of Physics
The Australian National University
Canberra Acton 2601, Australia

**ADVANCED
SCIENCE NEWS**

www.advancedsciencenews.com

www.lpr-journal.org

LASER
& PHOTONICS
REVIEWS

wearable devices, varifocal lenses,[26,27] and so forth.[28] They are expected to provide extreme wavefront molding versatility, opening up a broad scope of applications. When tuning the MS, it is of paramount importance to actively correct for the impact of fabrication imperfections and near-field coupling between nanostructures. Such correction can drastically improve device performances, especially for devices operating in a non-local regime, however, it has not been demonstrated to date.

To realize active MS, two distinct approaches have been considered so far. The first relies on addressing the pixel-by-pixel dynamical material response to adapt the device's optical properties via distributed external stimuli.[29,30] The second approach relies on mechanical, electrical, and chemical actuation to directly tune the whole MS.[27,31,32–34] This second approach, however, cannot provide arbitrary wavefront reconfigurability. We, therefore, focus on the first approach, as we are searching for an ideal pixel-by-pixel tunable meta-MS with high efficiency. Maximizing the transmission or reflection across the entire modulation range is not a straightforward task when operating at the nanoscale. Key challenges include poor electromagnetic field confinement, the difficulty in independently addressing each element, and the extremely weak modulation effect caused by the short interaction distance (typically on the order of a μm-thick). To circumvent these problems, choosing the right combination between material and phase tuning mechanisms is necessary. Dynamic light modulation at metasurfaces has been proposed using various material platforms, including phase change materials (PCMs),[35–38] liquid crystals (LC),[28] thermo-optic (TO)[39] or electro-optic (EO) effects.[40] PCMs offer large refractive index modulation ($\Delta n \approx 1$) but exhibit significant losses in the VIS and NIR wavelength range. LCs benefit from high industrial maturity and large Δn (in the range of $0.1 - 0.3$, however, they have relatively slow ($\lesssim$,kHz) modulation speed. The TO effect could reach similar index modulation with faster speed, however, it could result in the overall heating of the sample, as it mainly relies on passive cooling. The EO effect exhibits fast modulation speed (> 1 GHz) however is accompanied by a tiny refractive index change, usually on the order of $\Delta n \approx 10^{-3}$. Because each of these mechanisms has a different refractive index modulation Δn, a different resonant configuration is required to achieve full 2π phase modulation.

The modulation speed is also a concern when dealing with active tuning. Therefore, achieving both fast and large phase tuning becomes particularly challenging. Here, we address this issue by employing optical metasurfaces of high-quality factor (high-Q) resonances. However, a full 2π phase modulation in such metasurfaces is generally accompanied by undesirable amplitude changes, which need to be mitigated. To better understand the optical modulation properties of high-Q resonant structures, we propose to analyze their responses in the complex frequency plane, and in particular by examining the position of their topological singularities, namely the resonances and the associated zeros of the reflection coefficient. We show how to manipulate and exploit the positions of singularities in the complex plane to achieve phase only modulation with almost unity amplitude. We exemplify this concept by theoretically studying a reflective Gires– Tournois (G-T) cavity.[41] We then exploit our theoretical findings to design highly efficient G-T active metasurfaces comprising either the thermo-optical effect in Si nanoridges or the

quantum confined Stark effect in multiple quantum wells heterostructured materials. Furthermore, a global optimization technique is employed to maximize the beam-forming response by accounting for non-local response and near-field coupling between neighboring structures.[42,43] Our work highlights the role played by topological singularities in the scattering response of nanostructures and proves that optimization methods are becoming mandatory to modulate light efficiently, in particular when dealing with devices operating in the strong non-local coupling regime.

2. Understanding and Exploiting the Reflection Singularities of Gires– Tournois Nanoresonators

Reasonably assuming that Fabry– Pérot (F-P), G-T, and metasurfaces are exchanging energy with their environment, they can similarly be considered as open linear physical systems that are well represented by a matrix connecting input and output fields through a linear response function. We explore the reflection coefficient of a theoretical F-P cavity in the complex frequency plane to theoretically investigate these devices in the presence of radiation losses. In this complex plane, the imaginary part of the frequency represents the absorption or scattering losses.[44] Our analysis is based on the study of the complex-valued zeros and poles of the reflection coefficient, which are topological phase singularities. The positions of these singularities greatly influence the phase and the amplitude of the reflection coefficient on the real axis. More precisely, our objective is to identify the parameter condition for which zeros and poles are separated by the real axis in the complex frequency plane. This configuration yields a 2π phase accumulation along the real frequency axis.[21] We then study the influence of the zero– pole relative position with respect to the real axis on the quality factor of the resonance.

It is relatively trivial to write the analytical expression for the reflection coefficient of an F-P cavity consisting of a lossless medium of refractive index n and thickness t, enclosed between two mirrors with different real value reflection coefficients, defined as r_2 for the lower and r_1 for the upper mirror, respectively.[41] Considering an input field E_{in} (we choose the sign convention as $e^{-i\omega t}$) normally incident on the cavity (**Figure 1**a), one can express the overall device's reflection coefficient r of the F-P cavity as[45]

$$r = E_r/E_{in} = (r_1 + r_2 e^{i\delta})/(1 + r_1 r_2 e^{i\delta}) \tag{1}$$

where δ denotes the phase accumulation in the cavity given by $\delta = 2\omega n t/c$. Here, ω is the operating frequency in a vacuum, c is the speed of light, and E_r is the reflected electromagnetic field. This quantity can be expanded on complex-valued poles and zeros using the Weierstrass factorization theorem,[46–51] where each factor depends on the frequencies of the singularities, that is, poles $\omega_{p,m}$ and zeros $\omega_{z,m}$. Based on our sign convention choice, $e^{-i\omega t}$, zeros could have both positive or negative imaginary parts depending on the parameter condition, while poles always have a negative imaginary part to satisfy causality. Hence, the Weierstrass factorization yields

$$r(\omega) = \prod_m \frac{\omega - \omega_{z,m}}{\omega - \omega_{p,m}} \tag{2}$$
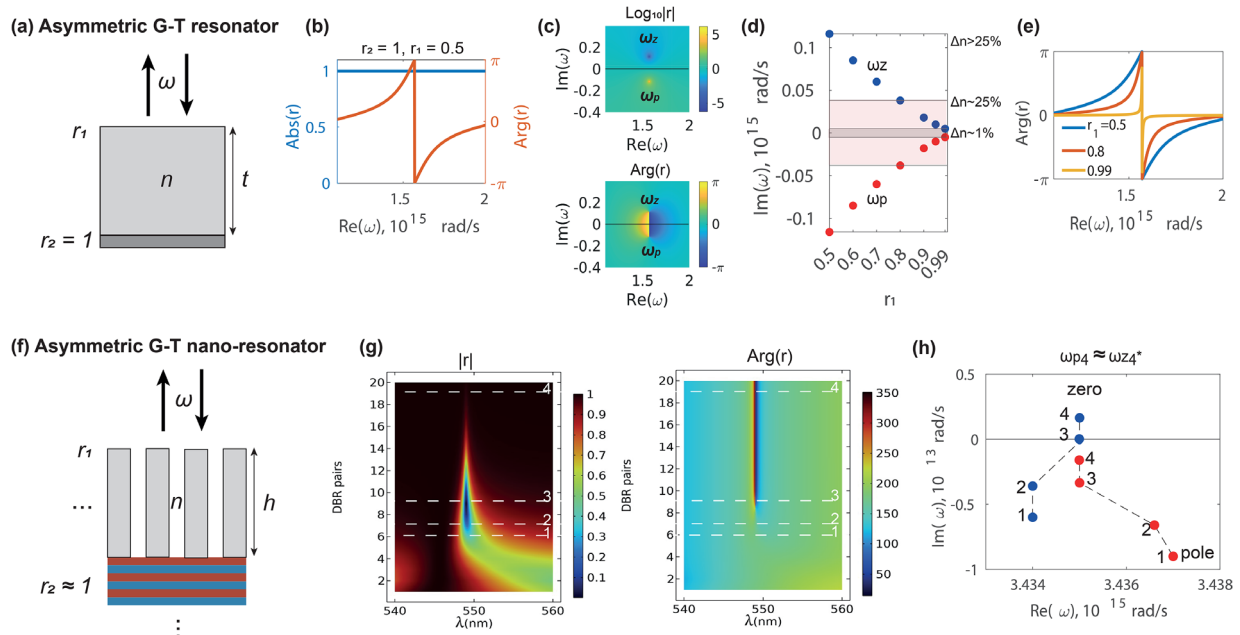
Figure 1. Theoretical description of a non-Hermitian G-T linear system and its analogy with a reflecting metasurface configuration. a) Schematic representation of a G-T resonator consisting of a layer of thickness t and refractive index n surrounded by two mirrors with reflection coefficients r_1 and r_2. b) Reflection amplitude and phase produced by the G-T cavity in (a) with $n = 1.5$, $t = 600$ nm, $r_2 = 1$, $r_1 = 0.5$. c) The amplitude and phase of the reflection coefficient, given the complex frequency in Equation (1), where the line $\text{Im}(\omega) = 0$ corresponds to the result in (b). d) Positions of the complex poles and zeros for a fixed reflectivity of the bottom mirror $r_2 = 1$ when the reflectivity of the top mirror r_1 is varied. As r_1 approaches unity, the zero–pole pairs approach the real axis, which increases the resonance quality factor. We identify the regions of the zero– pole pairs corresponding to different relative refractive index changes to achieve full 2π phase modulation in the tuning. e) The reflection phase corresponds to the result in (d) for different values of r_1. f) Schematic configuration of 2D GaN nanoridge (in gray) disposed in air and on the top of a distributed Bragg reflecting (DBR) mirror composed of HfO$_2$ ($n = 1.9$) and SiO$_2$ ($n = 1.47$) thin film pairs, as indicated by the blue and red layers, respectively. g) Color plot indicating reflection amplitude and the reflection phase evolution for light impinging at normal incidence as a function of the excitation frequency and the number of the DBR pairs. We observe the presence of a zero of reflection in the spectrum (i.e., at real frequencies) for about nine DBR pairs, that is, exactly when a phase singularity appears in the associated phase map. We indicate with numbered lines the number of DBR pair values for which the complex position of poles and zeros are numerically calculated and shown in (h). In panel (h), complex-valued reflection zeros and poles are shown as blue and red dots, respectively. For six and seven DBR pairs, both the zeros and poles lie below the real axis. For nine DBR pairs, the reflection zero reaches the real axis, as was already observed in panel (g). For 19 pairs, the zero moves to the upper part of the complex plane, separating the zero and pole on either side of the real axis, thus reaching the condition for full 2π-phase modulation, as confirmed in phase map in panel (g). Also, increasing the number of DBR pairs approaches r_2 closer to 1, thus reaching the G-T characterized by $\omega_\text{p} = \omega_\text{z}^*$ and corresponding to unity reflection amplitude. For all panels (f,g,h), the parameters of the GaN ridge are fixed with a width of 180 nm, a height of 200 nm, and $n_\text{GaN} = 2.38$.

where

$$\omega_{z,m} = (2m - 1)\frac{c\pi}{nt} - i\frac{c}{2nt}\log(r_1) + i\frac{c}{2nt}\log(r_2) \quad (3)$$

and

$$\omega_{p,m} = (2m - 1)\frac{c\pi}{nt} + i\frac{c}{2nt}\log(r_1) + i\frac{c}{2nt}\log(r_2) \quad (4)$$

Here m is an integer representing the cavity round-trip resonances. As r_1 and r_2 are real-valued and smaller than one, $\log(r_1)$ and $\log(r_2)$ are negative.

Equation (1) defines the position of the poles and zeros in a complex plane as a function of the reflectivity of the lower and upper mirrors. Thus, this expression completely determines the amplitude and the phase of the cavity response.[52] Let us consider only the case of a G-T cavity, that is, we assume a constant reflectivity of the lower mirror $r_2 = 1$ and keep a refractive index $n = 1.5$ and a thickness $t = 600$ nm for the rest of the theoretical derivation (see Figure 1a for more details). This choice

implies that a G-T cavity has only one incoming and one outgoing/reflecting channel. In this case, the scattering matrix reduces to a single coefficient, which is the reflection coefficient.[53] For a lossless system, the time-reversal symmetry is preserved so that the scattering poles and zeros are complex conjugates, that is, $\omega_\text{p} = \omega_\text{z}^*$ (see Equation (2) and refs. [50, 51]). This is theoretically confirmed by setting $r_2 \to 1$ in the expressions for $\omega_{z,m}$ and $\omega_{p,m}$, leading to complex conjugate zeros and poles for $r(\omega)$. Assuming ω to be complex in Equation (1) and plotting the reflection amplitude and phase in the complex frequency plane, we indeed observe two connected complex frequency singularities, as depicted in Figure 1b,c.

When the condition $\omega_\text{p} = \omega_\text{z}^*$ is fulfilled, the reflection coefficient features unity reflection amplitude and full 2π phase modulation when the real frequency varies from 0 to infinity (in fact, in a smaller frequency range as will be detailed later, in Figure 1e) as predicted analytically and shown in Figure 1b,c.

Once r_2 is set to unity, the upper mirror reflectivity, r_1 is used to control the quality factor of the resonance. Using the expression

for ω_z, m and ω_p, m, we theoretically predict the position and trajectories of the zero and pole singularities (zero–pole pairs) as a function of r_1, as shown in Figure 1d. Increasing r_1, that is, creating a cavity with a higher quality factor, decreases the absolute value of the imaginary parts of both singularities, corresponding to decreased losses. The losses vanish at the limit $r_1 = 1$, and the system becomes Hermitian with real eigenvalues. Considering the necessity of 2π phase modulation, we plot in Figure 1d the relative position of zeros and poles as a function of r_1, that is, as a function of the Q-factor of the cavity. It shows that the distance in the imaginary plane of a zero–pole pair of singularities decreases by increasing the quality factor. In Figure 1e, we present the evolution of the phase as a function of the real frequency with varying r_1. It shows that the phase modulation sharpens as a function of the frequency for increasing quality factor, thus correlating the phase modulation range with the imaginary value of the complex singularities. From our analysis of the G-T reflection in the complex frequency plane, the conditions for achieving full phase modulation and the unity efficiency are: zero–pole singularities have to be complex conjugated and their imaginary part has to be sufficiently small, that is, zero–pole have to be sufficiently close to each other, to experience rapid phase modulation as a function of the frequency.

Figure 1f illustrates the analogy made between a G-T resonator and an asymmetric metasurface resonator. The first design step consists in controlling the metasurface reflectivity to operate as a top G-T mirror through the excitation of low/high-quality resonance. We considered a single GaN resonator ($n = 2.38$) embedded in a vacuum and designed the structure to position the first magnetic dipole mode around $\lambda = 550$ nm. To mimic the G-T configuration, the resonator is then placed on top of a distributed Bragg reflector (DBR) composed of HfO_2/SiO_2 as shown in Figure 1f.

The reflection amplitude and phase maps as functions of the wavelength and the number of DBR pairs are presented in Figure 1g. When the reflectivity of the lower mirror increases (with an increasing number of DBR pairs), the presence of a reflection zero on the real axis is observed at approximately nine DBR pairs (line 3 in Figure 1g), that is, exactly when a phase singularity appears in the corresponding phase map panel. As for the GT-cavity, this behavior might be better understood by studying the positions of reflections zeros and poles in the complex plane. The locations of the complex-valued reflection zeros and poles are shown in Figure 1h. They were determined by performing numerical computations using the finite-element method based solver JCMsuite.[54] For a small reflectance of the lower mirror, both the zero (blue dot) and the pole (red dot) are located below the real axis, that is, both have negative imaginary parts. The corresponding phase does not vary much over the wavelength range displayed in Figure 1g, right plot. As the number of DBR pairs increases, the positions of zeros and poles move upward. For a given number of DBR pairs (nine in this example), the zero reflection amplitude reaches the real axis around the resonance wavelength ($\lambda = 550$ nm). This situation reflects the condition of critical coupling, corresponding to point 3 in Figure 1h, and becomes a reflectionless scattering mode (RSM).[53,55] This intersection of the reflection zero with the real axis corresponds to the zero region identified in Figure 1g.

Increasing further the number of DBR pairs, the zero moves into the upper part of the complex plane, while the pole remains confined under the real axis to satisfy the principle of causality. This condition leads to the appearance of the sharp 2π phase jump, see Figure 1g. The sufficient condition for a 2π phase accumulation related to the existence of the zero–pole pair separated by the real axis explains the phase behavior observed in Figure 1g for a number of DBR pairs larger than nine. Further increasing the bottom reflectivity yields a progressive increase in the reflection amplitude until the system reaches constant unity reflection. This corresponds, as expected, to the condition where zero and pole become complex conjugated of one another, see blue and red dots denoted 4 in Figure 1h.

Note that full-phase modulation for a similar geometry has been reported by tuning the geometrical parameters of a dielectric resonator on top of a highly reflective substrate.[45] 0 to 2π full phase addressing has been obtained using conventional real frequency excitation simulations.[45] Here we approach the problem from the complex frequency analysis, giving deeper insights and a rigorous physical explanation of the modulation properties. In the following, we will further exploit these results to conceive an active metasurface wavefront modulator, which is adjusted pixel-by-pixel to demonstrate high-performance active beam steering and deflection.

3. Electrically Tunable Gires–Tournois Metasurfaces

3.1. Thermo-Optical Tuning of the Light With Reflective Resonant Cavities

In this section, we propose an active MS modulation scheme that follows the recommendation derived in Section 2. It takes into consideration the physical requirements underlying the phase and unity amplitude modulation of the cavity resonance, that is, a unity reflectivity for the lower interface and a relatively sufficient high-Q resonance such that full phase modulation can be experienced using the thermo-optical effect in silicon (Si) nanoridges. We are concerned about experimental implementation and propose a simple design that can solve the fabrication challenges in tunable reflective G-T metasurfaces with ultimate performance. Silicon exhibits a relatively large thermo-optical effect, $\Delta n = \frac{dn}{dT}\Delta T$, that can be utilized to alter the metasurface scattering properties. Here, $\frac{dn}{dT}$ is the material thermo-optic coefficient. Previously, the thermo-optical effect of amorphous silicon has been exploited to introduce a sizable change in the refractive index of $\Delta n = 0.21$ by increasing its temperature from room temperature to 300 °C.[39,56] Aside from its large thermo-optic coefficient, the silicon's electrical properties allow it to be used as a resistive heater.[57,58] Here we use a ridge-metasurface design (**Figure 2**a), where each ridge serves as a localized resistive heater by applying a voltage across their end cross-sections. The generated heat in each ridge (and, therefore, its temperature) can be controlled by varying the current fed through the ridges.

Following the procedure in Section 2, we first consider a unit cell where a Si ridge is completely surrounded by SiO_2 and excited from the top with an x-polarized light, propagating in the z-direction. Figure 2a is a 3D schematic of the unit cell, invariant

**ADVANCED
SCIENCE NEWS**

www.advancedsciencenews.com

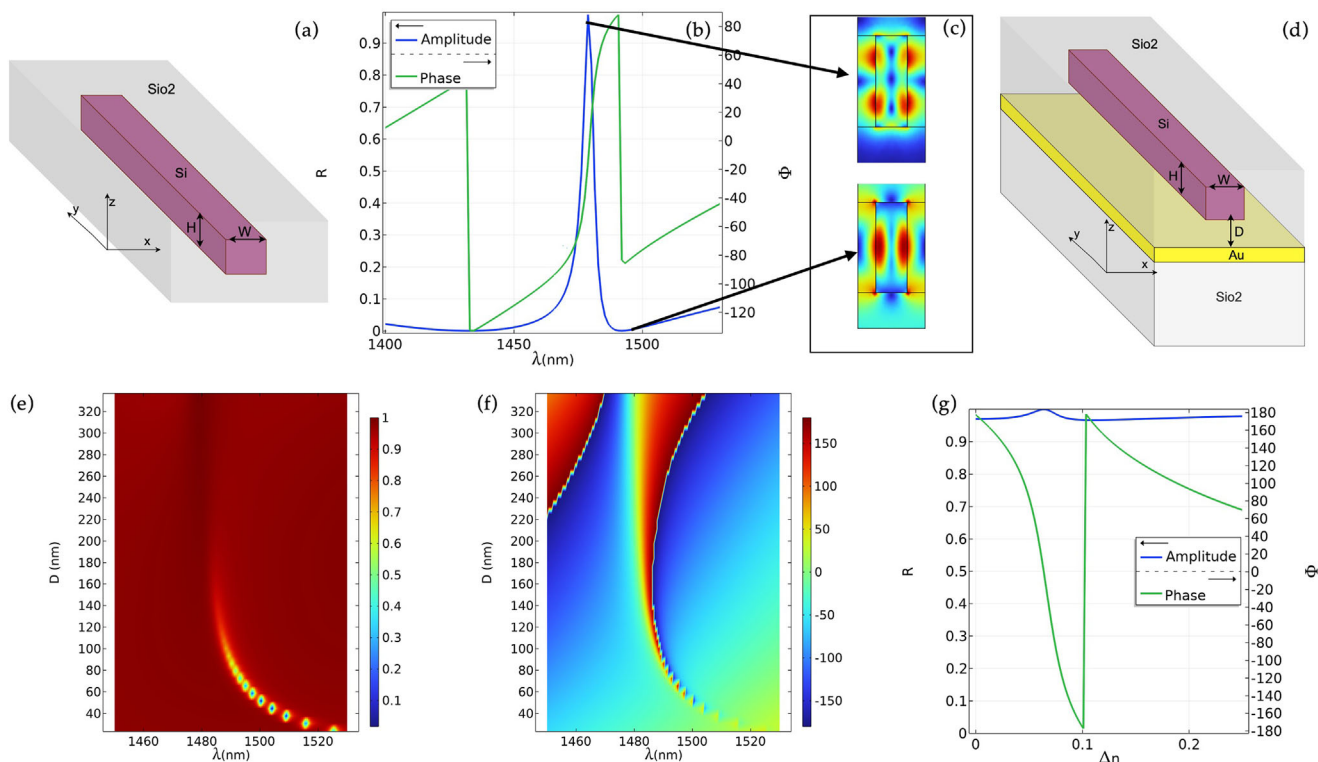LASER
& PHOTONICS
REVIEWS

www.lpr-journal.org

Figure 2. Schematic representation of an ideal active metasurface unit-cell based on thermo-optical effect to actively tune the reflected phase. Panels (a–c) refers to a Si unit-cell resonator surrounded by SiO$_2$, that is without a reflecting substrate and excited by a normally incident *x*-polarized light impinging from the top, whereas (d–g) represents the same resonator disposed on a thin gold layer of thickness 200 nm. The excitation also consists of an *x*-polarized beam coming at normal incidence. A homogeneous Sio$_2$ encapsulates a Si nano-ridge with dimensions of $H = 810$ nm and width $W = 280$ nm (a). The period of the unit cell is fixed at 600 nm, and the width and the thickness have been optimized to observe a sharp feature in the reflection spectrum around the desired wavelength of $\lambda = 1500$ nm, as shown in (b). The corresponding cross-section of the electric field distribution (along the *x–z* plane) is shown in (c). d) To take advantage of the G-T phase modulation mechanism discussed earlier, the resonator is placed on a thin reflective gold layer (thickness 200 nm) separated from the Si nano-ridge by a distance D. The reflection response amplitude and phase maps as a function of the distance D and the wavelength λ are depicted in (e,f). Increasing the value of D results in nearly 100% of the reflection amplitude with a $2pi$ phase response, in agreement with the expected ideal G-T functionality discussed in Section 2. Panel (f) depicts the reflected amplitude and phase modulation as a function of refractive index change. The latter is considered to be tuned via an external thermal stimulus with a maximum of $\Delta n = 0.25$ at the operation wavelength $\lambda = 1500$ nm.

in the *y*-direction. The width W and thickness H are optimized to achieve high modal confinement in the Si region for the designed wavelength of $\lambda = 1500$ nm. A sharp resonant response is realized in the reflection spectrum, as shown in Figure 2b,c. The unit-cell period in Figure 2b has been set as $P = 600$ nm, while the width W and the thickness H are fixed at 280 and 810 nm, respectively. The refractive index of Si at low temperatures is fixed at 3.48. After identifying the standalone resonant properties of the nano-ridge array, we place the unit-resonator on the top of a reflective gold layer (of thickness 200 nm). To achieve G-T reflectivity conditions and avoid light trapping in the gold layer, we vary the distance D (Figure 2d) between the Si nano-ridge and the gold layer. As shown in Figure 2e,f, as the distance D increases, the reflection amplitude increases to near unity, associated with a 2π phase modulation. In other words, the reflection zero converges to the condition of complex conjugation with its pole. Figure 2g finally shows the response of an active G-T unit cell with fixed geometric parameters and modulating the Si refractive index between 0 and 0.25. As seen, one achieves unitary reflection as well as over a 2π phase variation.

Further assembling a periodic arrangement of several of these ideal unit-cells presented in Figure 2d, we design an efficient thermally programmable beam steering device. The results presented in **Figure 3**a– c,d–f corresponds to the periodic electrical activation of six and four pixels, respectively, by applying a programmable pixel-by-pixel temperature control. In Figure 3a, each Si pixel is subjected to an individual potential difference, resulting in a different refractive index modulation. Due to the sub-wavelength pixel size, the reflected beam will be directed to the first diffraction order, according to the generalized law of reflection.[1] The main objective is then to maximize the light directed in the +1 lobe, that is, to find the Δn value for each Si ridge to steer the normally incident light in the desired direction with unity efficiency. Optimization can also be used to account for the strong near-field coupling between unit cells induced by the resonances. It is important to note that independent of the specific modulation technique, the overall performances of the fabricated metasurfaces remained relatively low, with wavefront addressing efficiency often below 70%, even for devices operating near their optimal design condition. The MS building blocks can be finely
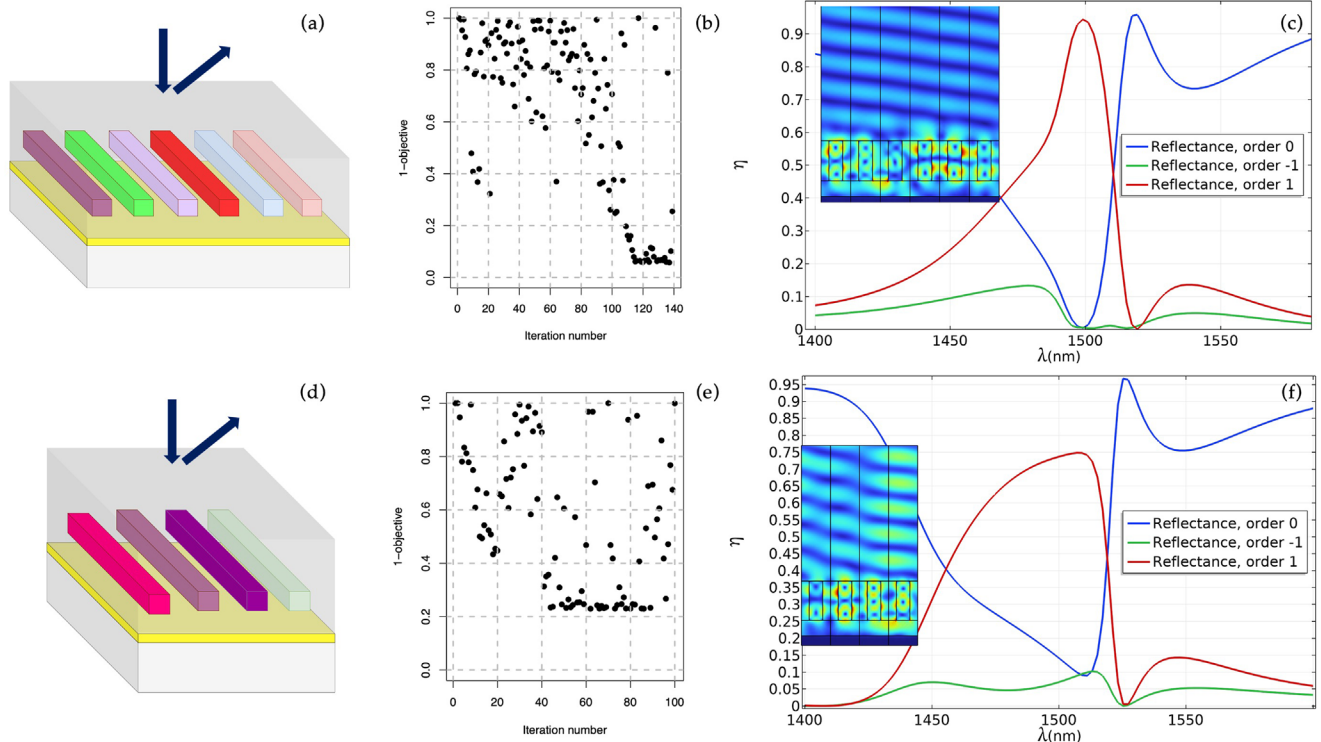
Figure 3. Active beam steering using an array of active G-T Si nanoresonators. Periodic electrical activation of a) six and d) four unit cells with pixel-by-pixel refractive index modulation. The optimization results for each case are depicted in (b,e), respectively. The beam steering responses after the optimized refractive index distribution in the sequential pixels are shown in panels (c,f) for six- and four-pixels configuration, respectively, with the corresponding field map at the design wavelength $\lambda = 1500$ nm. The optimization parameters represent the refractive index distribution in each pixel represented by different colors in (a) and (d). The corresponding refractive index values are given in Table 1.

tuned to take near-field coupling between adjacent elements and local changes in the MS surrounding environment into account. These effects are particularly noticeable in MS operating in the nonlocal regime, with strongly resonant nano-cells.[23,59–63]

We would like to emphasize that in our designs we attain full phase modulation associated with almost 100% reflection amplitude through single-unit cell simulation. Nonetheless, the resonance feature of the nonlinear phase modulation renders it arduous to engineer a high-performance beam deflector via the conventional lookup table synthesizing technique. To overcome this challenge, an advanced optimization strategy that accounts for near-field coupling effects between adjacent pixels is essential. Neglecting this coupling can result in significant degradation of the deflector's efficiency and accuracy. A critical aspect of our work is the consideration of the near-field coupling effects between adjacent elements in all the figures pertaining to beam steering or beam splitting, whether in the main text or Supporting Information section. This accounts for the impact of the local electromagnetic environment on the device performance and is a key point of emphasis in our manuscript. The accurate choice of the refractive index distribution among the repeated unit pixels is realized here by relying on an advanced optimization method known as efficient global optimization (EGO), specifically targeting the design of the metasurfaces.[5,42,43,64] In EGO, a surrogate model is used to statistically select the best candidates for the next simulation of the system. The optimization results (for the six-pixel case) are depicted in Figure 3b. The refractive index values

Table 1. Optimized values of the Si refractive index modulation (Δn) in each unit cell to diffract light on the first order only with maximal efficiency. The second and third columns correspond to the active metasurface unit cells composed of six and four pixels as depicted in Figure 3a,d, respectively.

Modulation	Six pixels	Four pixels
Δn_1	0.1188	0
Δn_2	0.1621	0.08133
Δn_3	0.250	0.150
Δn_4	0.0068	0.25
Δn_5	0.020	-
Δn_6	0.0541	-

required for efficient beam-steering have been optimized after only 100 iterations, illustrating the potential of EGO for fast optimization of metasurface's performances.

The illustrations in Figure 3a,d present the variation of the refractive index, as it is intuitively expected to design a blazed grating. The numerical optimization, however, yields a non-linear and even a non-monotonous variation of the refractive index along the pixels, as shown in **Table 1** and the corresponding phase map, given in Figure 2g. This is due to the strong near-field coupling between pixels. As illustrated in Figure 3c, the optimal − parameters (voltage distribution or extraordinary refractive index

modulation) yield a maximum of reflected power directed to the +1 order with an efficiency exceeding 93% with a 33° field of view (FoV). A similar optimization has been performed for periodic arrangements of four pixels, leading to 75% beam steering efficiency in the +1 order in Figure 3f with a higher steering angle of 50° FoV, as illustrated in Figure 3d–f. The optimization results after 100 iterations for this second case are given in Figure 3e. As indicated in the second column of Table 1, non-trivial refractive index distribution is required to mitigate the near-field coupling between pixels. To the best of our knowledge, this is the highest performance obtained so far for an active beam steering device using a simple configuration in reflection.[65]

3.2. Toward GHz Beam Steering Using the Electro-Optic Effect in a Quantum-Confined Stark Light Modulator

Tunable metasurfaces exploiting electro-optical effects have been proposed for dynamic wavefront engineering delivering exceptionally high modulation frequencies, up to the GHz range.[40] In this section, we propose an ultra-fast dynamic wavefront shaping metasurface operating in reflection using an electro-optic III–V MQW modulator.[63] The optical response of the MQW, particularly the refractive index, can be continuously tuned by applying an external voltage. Confined electron and hole levels in the QW are shifted in energy by the electric field via the so-called quantum confined stark Effect (QCSE).[66,67] The associated shift of the absorption edge leads to a change in the refractive index, which is the maximum for photon energies near the absorption band edge. With QCSE, the modulation frequency is theoretically limited by the dielectric relaxation rate and practically limited by RC terms that have to be minimized in the design and fabrication. Modulation frequencies up to the GHz frequency range can be envisioned. For QCSE modulation, the latter is generally within the 2%, which was previously the bottleneck for achieving highly efficient design.[66,67] To minimize losses, one has to operate at photon energy below the absorption edge but not too far below to keep a large index modulation. Moreover, experimental observation of GHz modulation speed would require minimizing the parasitic RC constants as the latter certainly exceeds the intrinsic dielectric relaxation rate.

Recently, ref. [63] reported on an active metasurface based on electro-optically tunable AlGaAs/GaAs MQW supporting hybrid Mie-guided mode resonance at $\lambda = 915$ nm. In their work, the MQW yields a maximum refractive index modulation of $\Delta n = 0.01$. A specific unit cell with high-quality Mie-guided mode resonance was considered to achieve a maximum phase modulation of 70° with 30% reflection amplitude in the vicinity of the refractive index modulation of $\Delta n = 0.01$. Accordingly, an active beam splitter with modest power and overall efficiency of less than 10% is realized at $\lambda = 915$ nm. Very recently, a numerical work realizing high-performance active metasurfaces by exploiting the linear electro-optic effect in lithium niobate (LiNbO$_3$) with a $\Delta n \approx 0.07$ index modulation has been proposed.[68] The structure consists of elongated nano-bars composed of Silicon (Si) on LiNbO$_3$, placed between two planar indium-tin-oxide (ITO) electrodes. High-Q guided mode resonances (GMR) leading to full 2π phase modulation are realized by adding sub-wavelength periodic notches parallel to the nanobar periodicity. In this section,

we consider an MQW heterostructure similar to the one used in ref. [63], that is, with a refractive index modulation of $\Delta n = 0.01$, and report on efficient sub-wavelength pixels featuring performances comparable with the latest state-of-the-art.

The proposed sub-wavelength pixel is shown in **Figure 4**a, where an active MQW region is encapsulated between two horizontal conductive electrodes. As previously discussed, high-Q metasurface elements are designed to exhibit significant optical modulation across a refractive index modulation of $\Delta n = 0.01$. Similar to Section 3.1, we consider a single unit cell surrounded by vacuum and tune the thickness H and the width W to produce a high-quality resonant mode confined in the MQW region (the amplitude and phase responses together with the field profiles are given in Figure S3a,b, Supporting Information). The presence of top and bottom contact electrodes introduces an impedance mismatch responsible for Fabry–Perot resonance inside the pillar. A uniform reflection amplitude and full phase accumulation as a function of the incident wavelength within a narrow wavelength range, as described in Section 2, are again obtained by adding a reflective lower DBR mirror consisting of SiO$_2$/HfO$_2$ pairs (see Figure 4a). The evolution of the phase and amplitude as a function of the reflectivity of the lower mirror (DBR pairs) is presented in the supplementary information (see Figure S3d, Supporting Information), where the G-T condition is observed for over 12 DBR pairs. Achieving 2π-phase accumulation in such a small wavelength range is needed to address a large phase variation as a function of the refractive index modulation for a fixed design wavelength, as demonstrated in Figure 4b.

We have exploited the ideal sub-wavelength pixels numerically to design high-efficiency programmable beam splitters. We considered programmable beam splitter designs with binary voltage to alter the deflection angle (in ±1 orders) as a function of period and applied voltages, as shown in Figure 4c,d. The expected overall efficiency reaches 90% and 80% with a FoV of 40° and 60°, respectively. It is worth noting that the binary phase distribution produced by the optimization is counter-intuitive (see Figure S4, Supporting Information) but still provides the highest beam-splitting power at the desired wavelength by accounting for strong near-field coupling. This ultimate performance, based on a realistic configuration and considering simple geometric features with a refractive index modulation of $\Delta n \approx 0.01$, demonstrates our design's potential for ultrafast beam steering.

4. Conclusion

In conclusion, we propose a simple methodology to design active metasurfaces operating in reflection. We studied the complex frequency response of a generic Fabry–Perot resonator, namely the position of zeros and poles of the reflection coefficient in the complex frequency plane. Using this approach, we have identified the conditions required to design an efficient tunable cavity. We conclude that i) unity reflection requires a conjugated pair of zero–pole singularities and ii) their imaginary part has to be chosen accordingly to the modulation depth, that is zero and pole have to be sufficiently close to each other such that the reflection experience a full phase modulation, as a function of the material modulation depth. We implement these conditions to demonstrate that light reflecting from a G-T resonator may undergo a strong resonant full non-linear 2π phase modulation with near unity reflection.
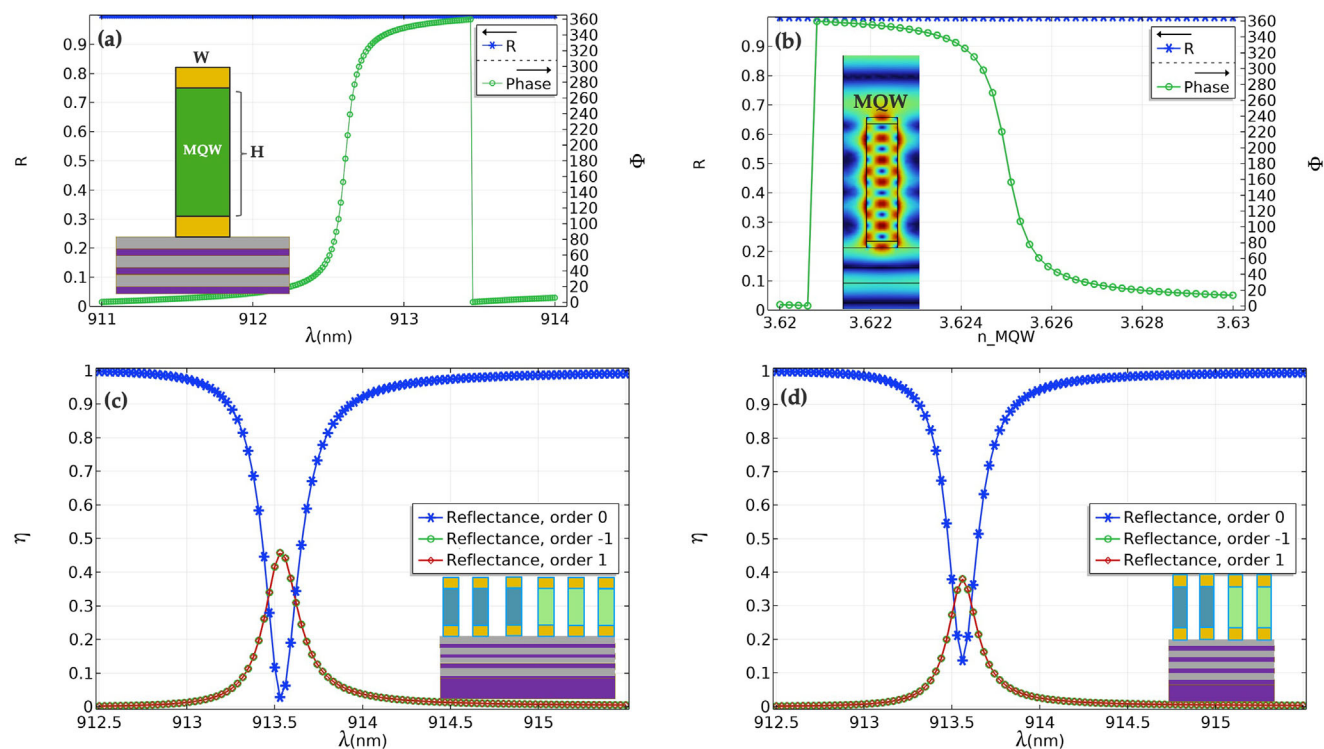
Figure 4. Ultra-fast programmable beam splitting relying on quantum-confined Stark modulation in an MQW heterostructure. a) The reflection phase and amplitude for the optimized sub-wavelength pixel. The x–z cross section of the considered single-unit cell is depicted in the inset (the structure is invariant in the y-direction). The active MQW (green region) is encapsulated between two conductive electrodes (here, we have considered p-doped GaAs). The resonator is placed on a DBR made of SiO_2/HfO_2 pairs (gray/purple sequences) on top of HfO_2 substrate. The geometrical parameters are as follows: $P = 450$ nm, width $w = 180$ nm, and thickness $H = 910$ nm. Besides, the thicknesses of the two electrodes are fixed as 50 nm with a refractive index of 3.55, and the effective refractive index of the MQW is chosen as in ref. [63] as 3.62. The response of the single unit cell without the DBR is presented in Figure S3, Supporting Information. b) Efficient metasurface response at $\lambda = 913.5$ nm upon the application of the external voltage across the MQW (the inset refers to the electric field distribution into the resonator for $v = 0$). c,d) Programmable active beam splitting with six (c) and four (d) pixels designed to deflect light at FoV of 40° and 60°, respectively. The refractive index distribution is given in Section S4, Supporting Information.

The resonant phase can be modified by varying the cavity thickness, the operation frequency, or the refractive index of interest, thus leading to active phase tuning. Classical phase gradient designs, relying on conventional look-up tables, are not necessarily leading to efficient beam forming. We observed that the strong resonant character of the excited optical modes magnifies further the near-field coupling effect between the resonators. We rely on a global optimization strategy to tackle this problem and demonstrate a considerable improvement in the MS beam-steering efficiency at each deflection angle. Two realistic designs consisting of semiconductor G-T cavities exploiting either thermo-optical effects in Si nano-cells or electro-optical effect in multiple quantum wells structures have been considered to demonstrate active deflection and beam steering at extreme field-of-view with ultimate performance exceeding 90%.

The design of active metasurfaces relying on materials presenting non-isotropic material response, generally characterized by a dielectric tensor, for example, one could consider liquid crystals, requires additional care. Indeed, the resonant nature of the GT mode considered herein provides both transverse and longitudinal field distributions, along x- or y- depending on the input polarization but also along the z-direction oriented along the propagation. The optimization of the deflector operating with

such anisotropic materials offers new and interesting perspectives of research and applications beyond the content of this manuscript. Our results also open up new and realistic perspectives for the conception of tunable metasurfaces with unexpected high frequency and high amplitude modulation capabilities for LiDARs and reconfigurable wavelength-division multiplexers in optical networks.

Supporting Information

Supporting Information is available from the Wiley Online Library or from the author.

Conflict of Interest

The authors declare no conflict of interest.

Data Availability Statement

The data that support the findings of this study are available from the corresponding author upon reasonable request.

Keywords

[1] N. Yu, P. Genevet, M. A. Kats, F. Aieta, J. P. Tetienne, F. Capasso, Z. Gaburro, *Science* **2011**, *334*, 333.

[2] P. Genevet, F. Capasso, F. Aieta, M. Khorasaninejad, R. Devlin, *Optica* **2017**, *4*, 139.

[3] S. Astilean, P. Lalanne, P. Chavel, E. Cambril, H. Launois, *Opt. Lett.* **1998**, *23*, 552.

[4] D. Lin, P. Fan, E. Hasman, M. L. Brongersma, *Science* **2014**, *345*, 298.

[5] M. M. Elsawy, A. Gourdin, M. Binois, R. Duvigneau, D. Felbacq, S. Khadir, P. Genevet, S. Lanteri, *ACS Photonics* **2021**, *8*, 2498.

[6] S. Wang, P. C. Wu, V. C. Su, Y. C. Lai, M. K. Chen, H. Y. Kuo, B. H. Chen, Y. H. Chen, T. T. Huang, J. H. Wang, R.-M. Lin, C.-H. Kuan, T. Li, Z. Wang, S. Zhu, D. P. Tsai, *Nat. Nanotechnol.* **2018**, *13*, 227.

[7] W. T. Chen, A. Y. Zhu, V. Sanjeev, M. Khorasaninejad, Z. Shi, E. Lee, F. Capasso, *Nat. Nanotechnol.* **2018**, *13*, 220.

[8] M. Pan, Y. Fu, M. Zheng, H. Chen, Y. Zang, H. Duan, Q. Li, M. Qiu, Y. Hu, *Light: Sci. Appl.* **2022**, *11*, 195.

[9] Q. Song, A. Baroni, R. Sawant, P. Ni, V. Brandli, S. Chenot, S. Vézian, B. Damilano, P. de Mierry, S. Khadir, P. Ferrand, P. Genevet, *Nat. Commun.* **2020**, *11*, 2651.

[10] Y. Y. Xie, P. N. Ni, Q. H. Wang, Q. Kan, G. Briere, P. P. Chen, Z. Z. Zhao, A. Delga, H. R. Ren, H. D. Chen, C. Xu, P. Genevet, *Nat. Nanotechnol.* **2020**, *15*, 125.

[11] P. Lalanne, S. Astilean, P. Chavel, E. Cambril, H. Launois, *JOSA A* **1999**, *16*, 1143.

[12] M. Khorasaninejad, F. Capasso, *Nano Lett.* **2015**, *15*, 6709.

[13] Z. Bomzon, G. Biener, V. Kleiner, E. Hasman, *Opt. Lett.* **2002**, *27*, 1141.

[14] M. Khorasaninejad, K. B. Crozier, *Nat. Commun.* **2014**, *5*, 5386.

[15] M. Khorasaninejad, W. T. Chen, R. C. Devlin, J. Oh, A. Y. Zhu, F. Capasso, *Science* **2016**, *352*, 1190.

[16] Y. Tian, X. Jing, H. Yu, H. Gan, C. Li, Z. Hong, *Opt. Express* **2020**, *28*, 32107.

[17] W. Liu, Y. S. Kivshar, *Opt. Express* **2018**, *26*, 13085.

[18] Y. F. Yu, A. Y. Zhu, R. Paniagua-Domínguez, Y. H. Fu, B. Luk'yanchuk, A. I. Kuznetsov, *Laser Photonics Rev.* **2015**, *9*, 412.

[19] L. Huang, X. Chen, H. Mühlenbernd, H. Zhang, S. Chen, B. Bai, Q. Tan, G. Jin, K. W. Cheah, C. W. Qiu, J. Li, T. Zentgraf, S. Zhang, *Nat. Commun.* **2013**, *4*, 2808.

[20] M. S. Bin-Alam, O. Reshef, Y. Mamchur, M. Z. Alam, G. Carlow, J. Upham, B. T. Sullivan, J. M. Ménard, M. J. Huttunen, R. W. Boyd, K. Dolgaleva, *Nat. Commun.* **2021**, *12*, 974.

[21] R. Colom, E. Mikheeva, K. Achouri, J. Zuniga-Perez, N. Bonod, O. J. Martin, S. Burger, P. Genevet, *arXiv:2202.05632*, **2022**.

[22] E. Mikheeva, C. Kyrou, F. Bentata, S. Khadir, S. Cueff, P. Genevet, *ACS Photonics* **2022**, *9*, 1458.

[23] J. Park, B. G. Jeong, S. I. Kim, D. Lee, J. Kim, C. Shin, C. B. Lee, T. Otsuka, J. Kyoung, S. Kim, K.-Y. Yang, Y.-Y. Park, J. Lee, I. Hwang, J. Jang, S. H. Song, M. L. Brongersma, K. Ha, S.-W. Hwang, H. Choo, B. L. Choi, *Nat. Nanotechnol.* **2021**, *16*, 69.

[24] I. Kim, R. J. Martins, J. Jang, T. Badloe, S. Khadir, H. Y. Jung, H. Kim, J. Kim, P. Genevet, J. Rho, *Nat. Nanotechnol.* **2021**, *16*, 508.

[25] R. Juliano Martins, E. Marinov, M. Youssef, C. Kyrou, M. Joubert, C. Colmagro, V. Gâté, C. Turbil, P. M. Coulon, D. Turover, S. Khadir, M. Giudici, C. Klitis, M. Sorel, P, Genevet, *Nat. Commun.* **2022**, *13*, 5724.

[26] C. Y. Fan, T. J. Chuang, K. H. Wu, G. D. J. Su, *Opt. Express* **2020**, *28*, 10609.

[27] E. Arbabi, A. Arbabi, S. M. Kamali, Y. Horie, M. Faraji-Dana, A. Faraon, *Nat. Commun.* **2018**, *9*, 812.

[28] S. Q. Li, X. Xu, R. Maruthiyodan Veetil, V. Valuckas, R. Paniagua-Domínguez, A. I. Kuznetsov, *Science* **2019**, *364*, 1087.

[29] H. Weigand, V. V. Vogler-Neuling, M. R. Escalé, D. Pohl, F. U. Richter, A. Karvounis, F. Timpu, R. Grange, *ACS Photonics* **2021**, *8*, 3004.

[30] J. Sautter, I. Staude, M. Decker, E. Rusak, D. N. Neshev, I. Brener, Y. S. Kivshar, *ACS Nano* **2015**, *9*, 4308.

[31] R. Kaissner, J. Li, W. Lu, X. Li, F. Neubrech, J. Wang, N. Liu, *Sci. Adv.* **2021**, *7*, eabd9450.

[32] C. Meng, P. C. Thrane, F. Ding, J. Gjessing, M. Thomaschewski, C. Wu, C. Dirdal, S. I. Bozhevolnyi, *Sci. Adv.* **2021**, *7*, eabg5639.

[33] C. A. Dirdal, P. C. Thrane, F. T. Dullo, J. Gjessing, A. Summanwar, J. Tschudi, *Opt. Lett.* **2022**, *47*, 1049.

[34] Q. He, S. Sun, L. Zhou, *Research* **2019**, *2019*, 1849272.

[35] S. Cueff, J. John, Z. Zhang, J. Parra, J. Sun, R. Orobtchouk, S. Ramanathan P. Sanchis, *APL Photonics* **2020**, *5*, 110901.

[36] Y. Zhang, C. Fowler, J. Liang, B. Azhar, M. Y. Shalaginov, S. Deckoff-Jones, S. An, J. B. Chou, C. M. Roberts, V. Liberman, M. Kang, C. Ríos, K. A. Richardson, C. Rivero-Baleine, T. Gu, H. Zhang, J. Hu, *Nat. Nanotechnol.* **2021**, *16*, 661.

[37] S. Lepeshov, A. Krasnok, *Nat. Nanotechnol.* **2021**, *16*, 615.

[38] S. Cueff, A. Taute, A. Bourgade, J. Lumeau, S. Monfray, Q. Song, P. Genevet, B. Devif, X. Letartre, L. Berguiga, *Adv. Opt. Mater.* **2021**, *9*, 2001291.

[39] M. Rahmani, L. Xu, A. E. Miroshnichenko, A. Komar, R. Camacho-Morales, H. Chen, Y. Zárate, S. Kruk, G. Zhang, D. N. Neshev, Y. S. Kivshar, *Adv. Funct. Mater.* **2017**, *27*, 1700580.

[40] I. C. Benea-Chelmus, S. Mason, M. L. Meretska, D. L. Elder, D. Kazakov, A. Shams-Ansari, L. R. Dalton, F. Capasso, *Nat. Commun.* **2022**, *13*, 3170.

[41] F. Gires, P. Tournois, *C. R. Acad. Sci.* **1964**, *258*, 6112.

[42] M. M. Elsawy, M. Binois, R. Duvigneau, S. Lanteri, P. Genevet, *Opt. Express* **2021**, *29*, 29887.

[43] M. M. Elsawy, S. Lanteri, R. Duvigneau, G. Brière, M. S. Mohamed, P. Genevet, *Sci. Rep.* **2019**, *9*, 17918.

[44] H. M. Nussenzveig, *Causality and Dispersion Relations*, Academic Press, Cambridge, MA **1972**.

[45] S. Colburn, A. Zhan, A. Majumdar, *Sci. Rep.* **2017**, *7*, 40174.

[46] M. C. Hutley, D. Maystre, *Opt. Commun.* **1976**, *19*, 431.

[47] R. A. Depine, V. L. Brudny, J. M. Simon, *Opt. Lett.* **1987**, *12*, 143.

[48] L. C. Botten, M. Cadilhac, G. H. Derrick, D. Maystre, R. C. McPhedran, M. Neviere, P. Vincent, *Electromagnetic Theory of Gratings, Softcover reprint of the original 1st ed. 1980 Edition*, Springer, Berlin, Heidelberg **2011**.

[49] D. Maystre, *Theory of Wood's Anomalies, Plasmonics* (eds: S. Enoch, N. Bonod), Springer, Berlin, Heidelberg **2012**, pp. 39–83.

[50] V. Grigoriev, S. Varault, G. Boudarham, B. Stout, J. Wenger, N. Bonod, *Phys. Rev. A* **2013**, *88*, 063805.

[51] A. Krasnok, D. Baranov, H. Li, M. A. Miri, F. Monticone, A. Alú, *Adv. Opt. Photonics* **2019**, *11*, 892.

[52] E. A. Bezus, D. A. Bykov, L. L. Doskolovich, *Opt. Lett.* **2020**, *45*, 5065.

[53] W. R. Sweeney, C. W. Hsu, A. D. Stone, *Phys. Rev. A* **2020**, *102*, 063511.

[54] J. Pomplun, S. Burger, L. Zschiedrich, F. Schmidt, *Phys. Status Solidi B* **2007**, *244*, 3419.

[55] W. Yang, S. Sun, C. Zhang, J. Li, Z. Duan, Q. Song, S. Xiao, *Sci. Rep.* **2016**, *6*, 38964.

[56] K. Z. Kamali, L. Xu, J. Ward, K. Wang, G. Li, A. E. Miroshnichenko, D. Neshev, M. Rahmani, *Small* **2019**, *15*, 1805142.

[57] M. Jacques, A. Samani, E. El-Fiky, D. Patel, Z. Xing, D. V. Plant, *Opt. Express* **2019**, *27*, 10456.

[58] S. De, R. Das, R. K. Varshney, T. Schneider, *IEEE Access* **2020**, *8*, 141632.

[59] H. Cai, S. Srinivasan, D. A. Czaplewski, A. B. Martinson, D. J. Gosztola, L. Stan, T. Loeffler, S. K. Sankaranarayanan, D. López, *npj Comput. Mater.* **2020**, *6*, 116.

[60] C. Gigli, Q. Li, P. Chavel, G. Leo, M. L. Brongersma, P. Lalanne, *Laser Photonics Rev.* **2021**, *15*, 2000448.

[61] S. C. Malek, A. C. Overvig, A. Alù, N. Yu, *arXiv:2009.07054*, **2020**.

[62] A. C. Overvig, S. C. Malek, N. Yu, *Phys. Rev. Lett.* **2020**, *125*, 017402.

[63] P. C. Wu, R. A. Pala, G. Kafaie Shirmanesh, W. H. Cheng, R. Sokhoyan, M. Grajower, M. Z. Alam, D. Lee, H. A. Atwater, *Nat. Commun.* **2019**, *10*, 3654.

[64] M. M. Elsawy, S. Lanteri, R. Duvigneau, J. A. Fan, P. Genevet, *Laser Photonics Rev.* **2020**, *14*, 1900445.

[65] P. Thureja, R. Sokhoyan, C. U. Hail, J. Sisler, M. Foley, M. Y. Grajower, H. A. Atwater, *Nanophotonics* **2022**, *11*, 3745.

[66] J. Lee, S. Jung, P. Y. Chen, F. Lu, F. Demmerle, G. Boehm, M. C. Amann, A. Alù, M. A. Belkin, *Adv. Opt. Mater.* **2014**, *2*, 1057.

[67] Y. H. Kuo, Y. K. Lee, Y. Ge, S. Ren, J. E. Roth, T. I. Kamins, D. A. Miller, J. S. Harris, *Nature* **2005**, *437*, 1334.

[68] E. Klopfer, S. Dagli, D. Barton III, M. Lawrence, J. A. Dionne, *Nano Lett.* **2022**, *22*, 1703.